

# Multi-Shape Matching with Cycle Consistency Basis via Functional Maps

Yifan Xia<sup>1\*</sup>, Tianwei Ye<sup>1\*</sup>, Huabing Zhou<sup>2</sup>, Zhongyuan Wang<sup>3</sup>, Jiayi Ma<sup>1†</sup>

<sup>1</sup>Electronic Information School, Wuhan University, Wuhan 430072, China

<sup>2</sup>School of Computer Science and Engineering, Wuhan Institute of Technology, Wuhan 430205, China

<sup>3</sup>School of Computer Science, Wuhan University, Wuhan 430072, China

xiayifan@whu.edu.cn, twye2001@gmail.com, zhoubing@gmail.com, wzy\_hope@163.com, jyma2010@gmail.com

## Abstract

Multi-shape matching is a central problem in various applications of computer vision and graphics, where cycle consistency constraints play a pivotal role. For this issue, we propose a novel and efficient approach that models multi-shapes as directed graphs for two-stage optimization, i.e., optimizing pairwise correspondence accuracy using landmarks, and refining matching consistency through cycle consistency basis. Specifically, we utilize local mapping distortion to identify landmarks and extract the dimension of the functional space, which is then used to upsample in the spectral domain, thereby producing smoother results. Next, to optimize the consistency of correspondences, we introduce the cycle consistency basis, which succinctly describes all consistent cycles in the collection. We then propose cycle consistency refinement, which resolves inconsistencies in cycles efficiently via the alternating direction method of multipliers. Our approach simultaneously balances the accuracy and consistency of multi-shape matching, achieving lower correspondence errors. Extensive experiments on several public datasets demonstrate the superiority of our approach over current state-of-the-art methods.

Code — <https://github.com/YeTianwei/CyCoMatch>

## Introduction

Finding correspondences between non-rigid 3D shapes is a fundamental and critical task in computer vision and graphics (Van Kaick et al. 2011; Sahillioglu 2020), with applications in shape analysis (Hartman et al. 2023), texture transfer (Aigerman, Poranne, and Lipman 2015), and pose estimation (Jiang et al. 2022). Unlike correspondences between rigid shapes, which can be achieved through simple parameter deformations, correspondences between non-rigid shapes have to address more unpredictable deformations.

Near-isometric mappings between shapes have been widely studied due to the characteristics of approximately isometric deformations in the real world (Sahillioglu 2020). One highly emphasized approach is the functional maps framework (Ovsjanikov et al. 2012). By establishing correspondences between real-valued functions rather than

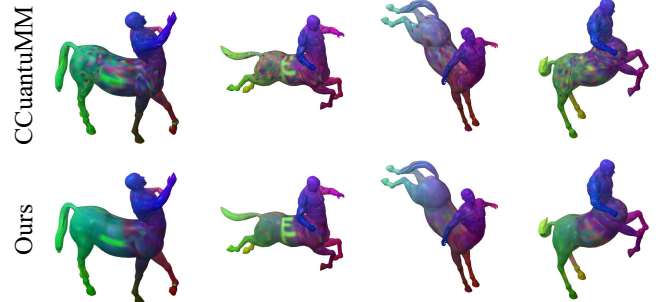


Figure 1: Example of a qualitative comparison between our method and the representative state-of-the-art multi-shape matching method CCuantuMM (Bhatia et al. 2023) using color transfer. Notably, our method demonstrates more accurate and consistent results.

points, functional maps represent the correspondence based on the spectral space of each shape, typically using the eigenfunctions of the Laplace-Beltrami operator. Subsequent works have significantly enhanced the accuracy (Kovnatsky et al. 2013; Nogneng and Ovsjanikov 2017), efficiency (Burghard, Dieckmann, and Klein 2017), and robustness (Rodolà et al. 2017) of the functional maps pipeline.

However, in practice, we often acquire multiple shapes in a collection, such as multiple poses of the same target, which naturally leads to the need for multi-shape matching (Van Kaick et al. 2011). Meanwhile, a fundamental challenge of shape matching is that the limited information between pairs of shapes restricts the accuracy of the generated mapping. By considering the information from multiple shapes, this problem can be effectively mitigated (Van Kaick et al. 2011). In multi-shape matching, there is also a natural constraint called *cycle consistency* (Huang and Guibas 2013; Huber 2002), which states that composite mapping along a cycle should be identity map. As a global map prior, cycle consistency has long been used to jointly improve the effectiveness of maps between multiple shapes. Considering the cycle consistency constraint is key to achieving successful multi-shape matching.

Given this background, many multi-shape matching methods focus on better-leveraging cycle consistency constraints to achieve higher-quality correspondences. Early ap-

\*These authors contributed equally.

†Corresponding author.

Copyright © 2025, Association for the Advancement of Artificial Intelligence (www.aaai.org). All rights reserved.

proaches combine cycle consistency with the low-rank characterization of matrices (Huang and Guibas 2013; Kezurer et al. 2015). Due to a lifting strategy that dramatically increases the number of variables, these methods do not scale well to large problems, resulting in only sparse correspondences. Subsequent methods impose cycle consistency constraints on pairwise functional maps (Shoham, Vaxman, and Ben-Chen 2019; Wang, Huang, and Guibas 2013) but neglect the spatial domain information of shapes (Huang, Wang, and Guibas 2014; Huang et al. 2019). Recent methods attempt to incorporate cycle consistency requirements explicitly into the optimization process (Bernard et al. 2019), but they are limited by the size of the problem, often down-sampling the number of shape points (Huang et al. 2020; Gao et al. 2021). This approach also results in the loss of local features and limits the effectiveness of matching.

Although several methods have recently been proposed to solve multi-shape matching with success, they consistently relate cycle consistency to the properties of matrices. For example, the low-rank property of matrices is exploited in CSM (Huang and Guibas 2013), functional mapping matrices are used to construct canonical consistent latent bases in Limit shapes (Huang et al. 2019), and permutation synchronization of matrices is directly addressed in Hippi (Bernard et al. 2019). However, all of these approaches ignore the inherent information within the natural graph structure of shape collection and fail to construct more concise cycle consistency constraints.

To mitigate these limitations, we model multiple shapes as directed graphs and perform a two-stage optimization for accuracy and consistency. Firstly, to get higher-quality pairwise correspondences, we introduce local mapping distortion to evaluate correspondence quality and identify landmark points, thereby avoiding the influence of low-quality points (i.e., non-landmarks) in current correspondences. After obtaining more accurate functional maps via landmarks, we refine them by extracting functional space dimensions and upsampling under spectral manifold wavelet constraints. This approach eliminates the need for empirical design of spectral embedding dimensions. Iterative dimension updates also overcome the limitations of fixed dimensions, resulting in smoother mappings. Subsequently, we perform cycle-consistency optimization on the pairwise correspondences. Observing the exponential magnitude, uncertainty, and complexity of the cycles, we introduce the cycle consistency basis, which succinctly describes all cycles that satisfy consistency within a shape collection. Finally, we propose cycle consistency refinement to eliminate inconsistencies in previous correspondences within cycles, and efficiently solve it using the Alternating Direction Method of Multipliers to obtain the final correspondences. We provide a qualitative comparison between our method and the recent multi-shape matching algorithm, CCuantuMM (Bhatia et al. 2023), in Fig. 1, to demonstrate our superiority. In summary, the three main contributions are as follows:

- We model multiple shapes as directed graphs and perform a two-stage optimization to ensure matching accuracy and consistency.

- We present the cycle consistency basis that intuitively and effectively constrains the cycle consistency of the functional mapping results.
- We demonstrate the superiority of our approach over the current state-of-the-art on multiple public datasets.

## Related Work

### Functional Maps

The 3D shape is modeled as a smooth and compact two-dimensional Riemannian manifold  $\mathcal{X}$ , embedded in  $\mathbb{R}^3$ . The space of square-integrable functions on the manifold  $\mathcal{X}$  is denoted as  $\mathcal{L}^2(\mathcal{X}) = \{f : \mathcal{X} \rightarrow \mathbb{R}, \int_{\mathcal{X}} f(x)^2 d\mu < \infty\}$ . Fourier analysis of the manifold  $\mathcal{X}$  is performed using the Laplace-Beltrami operator  $\Delta_{\mathcal{X}}$ . For  $i \geq 1$ , there exists an eigen-decomposition  $\Delta_{\mathcal{X}}\phi_i = \lambda_i\phi_i$ , with eigenfunctions  $\{\phi_i\}_{i \geq 1}$  as orthogonal bases and eigenvalues  $\{\lambda_i\}_{i \geq 1}$  as eigenvalues of  $\mathcal{L}^2(\mathcal{X})$ . Let the matrix  $\Phi_{\mathcal{X}} \in \mathbb{R}^{m \times k}$  denote the first  $k$  Laplace-Beltrami eigenfunctions of  $\mathcal{X}$ , where each column corresponds to an eigenfunction and each row corresponds to a point. We also denote  $\Lambda_{\mathcal{X}} = \text{diag}(\lambda_0^{\mathcal{X}}, \lambda_1^{\mathcal{X}}, \dots, \lambda_{k-1}^{\mathcal{X}})$  as the diagonal matrix containing the first  $k$  Laplace-Beltrami eigenvalues.

Given a pointwise map  $T : \mathcal{X} \rightarrow \mathcal{Y}$ , we consider a functional map  $T_F : \mathcal{L}^2(\mathcal{X}) \rightarrow \mathcal{L}^2(\mathcal{Y})$  that maps functions from  $\mathcal{L}^2(\mathcal{X})$  to  $\mathcal{L}^2(\mathcal{Y})$ . Thus, the result of mapping a function  $f \in \mathcal{L}^2(\mathcal{X})$  on  $\mathcal{X}$  is  $T_F(f) = f \circ T^{-1}$ . Next, using the Laplace-Beltrami orthogonal bases  $\{\phi_i^{\mathcal{X}}\}_{i \geq 0}$  and  $\{\phi_j^{\mathcal{Y}}\}_{j \geq 0}$ , the mapped result  $T_F(f)$  can be expressed as:

$$T_F(f) = \sum_j \sum_i \langle f, \phi_i^{\mathcal{X}} \rangle_{\mathcal{X}} \underbrace{\langle T_F(\phi_i^{\mathcal{X}}), \phi_j^{\mathcal{Y}} \rangle_{\mathcal{Y}}}_{c_{ji}} \phi_j^{\mathcal{Y}}. \quad (1)$$

We define  $C = [c_{ji}] \in \mathbb{R}^{k \times k}$  to represent the mapping between the first  $k$  eigenfunctions, which encodes the functional maps. To solve for the unknown matrix  $C$ , it is the standard practice to implement several linear constraints on  $C$ , such as constraints on preserving descriptors and the commutativity of the Laplace-Beltrami operator (Ovsjanikov et al. 2012). These constraints enable the functional maps to be obtained by solving a least squares system.

### Cycle Consistency Basis

The concept of cycle consistency basis is derived from the well-studied notion of cycle bases in directed graphs (Kavitha et al. 2009). A cycle basis comprises the smallest set of cycles in a graph, with any cycle representable as a linear combination of these bases. When extended to cycle consistency basis, this concept identifies the smallest set of cycles needed to enforce consistency across the entire graph (Guibas, Huang, and Liang 2019).

Specifically, consider a directed graph  $G = (V, E)$ , where each vertex  $v_i$  is linked with a domain  $D_i$  and each edge  $e = (i, j)$  involves a mapping  $f_{ij}$  from  $D_i$  to  $D_j$ . Define a composite mapping  $f_c = f_{i_1 i_2} \circ \dots \circ f_{i_k i_1}$  along a cycle  $c = (i_1, i_2, \dots, i_k, i_1)$  in  $G$ . This mapping is cycle consistent if it satisfies  $f_c = \text{Id}$  for every cycle  $c$  in a set  $\mathcal{C}$ . Given a cycle set  $\mathcal{C}$  and a cycle  $c \notin \mathcal{C}$ , we say that  $\mathcal{C}$  induces  $c$  if

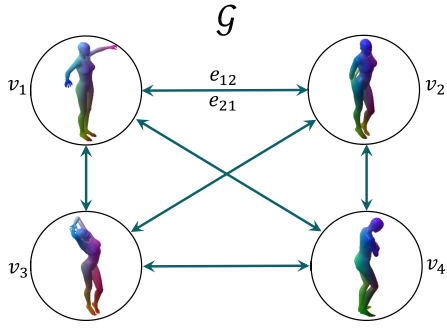


Figure 2: Example of a collection of shapes modeled as a directed graph  $\mathcal{G} = (\mathcal{V}, \mathcal{E})$ , where  $v_i \in \mathcal{V}$  represents shape  $S_i$  and  $e_{ij} \in \mathcal{E}$  denotes correspondence from  $S_i$  to  $S_j$ .

there exists an ordered set of cycles  $\{c_1, \dots, c_K\} \subseteq \mathcal{C}$  and intermediate cycles  $c^{(k)}$  ( $1 \leq k \leq K$ ), where  $c^{(1)} = c_1$ , and each  $c^{(k)}$  is formed by adding new edges from  $c_k$  to  $c^{(k-1)}$  and removing their common edges, i.e.,  $c^{(k)} = c^{(k-1)} \oplus c_k$ , ultimately forming the cycle  $c$  with  $c^{(K)} = c$ . Therefore, a cycle set  $\mathcal{C}$  is considered a cycle consistency basis if it induces all other cycles.

## Method

This section outlines our multi-shape matching in the functional maps framework, introducing cycle consistency basis as constraints. Starting with initial correspondences, we construct a directed graph to optimize the matching in two steps: (i) optimizing the accuracy of pairwise correspondences using landmarks, and (ii) refining the consistency of matching by generating cycle consistency basis from the graph.

### Pairwise Correspondences via Landmarks

We assume to be given a collection of shapes  $\mathcal{S} = \{S_i\}_{i=1}^n$  represented as triangular meshes with initial pointwise correspondences  $\{T_{ij}\}_{i,j=1}^{n,n}$ . We model  $\mathcal{S}$  as a directed graph  $\mathcal{G} = (\mathcal{V}, \mathcal{E})$ , as illustrated in Fig. 2. The first step is to optimize the accuracy of matches, using Local Mapping Distortion (LMD) to evaluate the quality of current matches and identify landmarks. For generality, we next discuss the correspondence on any edge  $e_{ij}$  between  $S_i$  and  $S_j$ .

**Landmarks Identification** The LMD is proposed for near-isometric shapes, allowing for mapping accuracy evaluation without ground truth by geodesic distance preservation (Xiang, Lai, and Zhao 2020, 2021). Let  $T: S_1 \rightarrow S_2$  denote the pointwise map between two shapes. The LMD of the map  $T$  at point  $x_i \in S_1$  can be expressed as:

$$\mathcal{D}_\gamma(T)(x_i) = \frac{\sum_{x_j \in \mathcal{B}_\gamma(x_i)} \mathcal{A}_1(j) DE_T(x_i, x_j)}{\sum_{x_j \in \mathcal{B}_\gamma(x_i)} \mathcal{A}_1(j)}, \quad (2)$$

where  $\mathcal{B}_\gamma(x_i) = \{x_j \in S_1 \mid d_{S_1}(x_i, x_j) \leq \gamma\}$  denotes the  $\gamma$ -geodesic ball of  $x_i$ ,  $\mathcal{A}_1$  is the area element of the mesh of shape  $S_1$ , and  $DE_T(x_i, x_j) = \frac{1}{\gamma} |d_{S_1}(x_i, x_j) - d_{S_2}(T(x_i), T(x_j))|$  represents the distortion in geodesic distance when mapping nearby points  $x_i$

---

### Algorithm 1: Pairwise Correspondences Refinement

---

**Input:** Shapes  $S_i, S_j$ , initial correspondence  $T_{ij}$   
**Parameter:** Maximum iterations  $MaxIt$ , LMD thresholds  $\{\epsilon_{it}\}_{it=1}^{MaxIt}$   
**Output:** Optimized  $C_{ij}$

```

1: while  $0 \leq it \leq MaxIt$  do
2:   Use Local Mapping Distortion to identify landmarks;
3:   Compute functional map using landmarks by Eq. (3);
4:   Extract dimension  $k_{it}$  of landmarks functional space;
5:   Reconstruct functional map by Eq. (7);
6:   Obtain final  $C_{ij}$  by Eq. (8);
7:   Transform  $C_{ij}$  to  $T_{ij}$  by NN search & encoded as  $\Pi$ ;
8: end while

```

---

and  $x_j$  to  $T(x_i)$  and  $T(x_j)$ . Smaller values of  $\mathcal{D}_\gamma(T)(x_i)$  indicate better continuity of the mapping  $T$  at  $x_i$ . Based on the definition of LMD, we can infer that  $\mathcal{D}_\gamma(T)(x_i) = 0$  when  $T$  is an ideally isometric mapping. Conversely, there exists some  $\gamma > 0$  such that  $\mathcal{D}_\gamma(T)(x_i) = 0$  when  $T$  is isometric.

By setting a threshold  $\epsilon$ , we identify a set of well-matched points  $\{(x_l, T(x_l)) \mid \mathcal{D}_\gamma(T)(x_l) \leq \epsilon\}$ , and call these landmarks  $\{x_l\}_{l=1}^m$ , where  $m$  is the number of selected points.

**Dimension Extraction** By leveraging landmarks  $\{x_l\}_{l=1}^m$ , we transform the initial  $T_{ij}$  into a functional mapping:

$$C_{ij}^l = \Phi_{S_i}(\{x_l\}_{l=1}^m)^\top \Pi \Phi_{S_j}(\{T_{ij}(x_l)\}_{l=1}^m), \quad (3)$$

where  $\Pi_{ij}$  is a permutation matrix encoded by  $T_{ij}$ . Then, based on the distribution of landmarks in the functional space, dimension  $k$  is extracted using principal components:  $U \Sigma V^\top = \Phi_{S_i}(\{x_l\}_{l=1}^m)^\top \Phi_{S_j}(\{T_{ij}(x_l)\}_{l=1}^m)$ . Due to the potential degradation,  $k$  is much smaller than the number of landmarks. We determine  $k$  by truncating when the changes in 10 consecutive singular values fall below 0.1.

The dimension  $k$  derived from landmarks avoids the need for empirical design or simple incremental changes typically required. It also prevents low-quality points (i.e., non-landmarks) from introducing errors during the subsequent upsampling process.

**Functional Map Reconstruction** After determining the dimensions of the landmark functional space, we reconstruct the functional space using functional maps constrained by multiscale spectral wavelets (Hu et al. 2021).

Given a smooth filter  $g(\lambda) : \mathbb{R}^+ \rightarrow \mathbb{R}^+$ , the spectral manifold wavelets at the scale  $s$  and point  $y$  are defined as:

$$\psi_{s,y}(x) = \sum_{i \geq 0} g(s\lambda_i) \phi_i^*(y) \phi_i(x). \quad (4)$$

To fully analyze the characteristics of a shape at different scales, the scale parameter  $s$  is typically sampled as a set of discrete points  $\{s_l\}_{l=0}^L$ , and  $L$  is a predefined scale number.

Then, we can derive two wavelet matrices  $\Psi_s^{S_i} = \Phi_{S_i} g(s\Lambda_{S_i}) \Phi_{S_i}^+$  and  $\Psi_s^{S_j} = \Phi_{S_j} g(s\Lambda_{S_j}) \Phi_{S_j}^+$  for shapes  $S_i$  and  $S_j$ . Therefore, the Fourier coefficient matrices of the wavelet matrices  $\Psi_s^{S_i}$  and  $\Psi_s^{S_j}$  are  $g(s\Lambda_{S_i}) \Phi_{S_i}^+$  and

$g(s\Lambda_{S_j})\Phi_{S_j}^+$ , respectively. In the case of functional space dimension  $k$ , we define the following optimization problem:

$$\begin{aligned} \min_{\Pi, C_k^r} \sum_{l=0}^L \left\| C_k^r g(s_l \Lambda_{S_i}^k) (\Phi_{S_i}^k)^+ - g(s_l \Lambda_{S_j}^k) (\Phi_{S_j}^k)^+ \Pi^\top \right\|_F^2, \\ \text{s.t. } \Pi \mathbf{1} = \mathbf{1}, \quad \Pi^\top \mathbf{1} \leq \mathbf{1}, \end{aligned} \quad (5)$$

where  $\mathbf{1}$  is an all-1 vector of the same dimension as  $\Pi$ . We simplify the problem by alternately optimizing  $C_k^r$  and  $\Pi$ , and introduce the analytic solution of  $C_k^r$  with fixed  $\Pi$ :

$$C_k^r g(s_l \Lambda_{S_i}^k) (\Phi_{S_i}^k)^+ = g(s_l \Lambda_{S_j}^k) (\Phi_{S_j}^k)^+ \Pi^\top. \quad (6)$$

Eq. (6) still involves solving a large number of linear systems. However, it can be simplified when a suitable set of filters is employed. Specifically, the wavelet set  $\{g(s_l \lambda)\}_{l=0}^L$  constitutes a Parseval framework (Leonardi and Van De Ville 2013) that satisfies  $\sum_s g^2(s\Lambda) = \mathbf{I}$ , resulting in the final solution:

$$C_k^r = \sum_{l=0}^L g(s_l \Lambda_{S_j}^k) (\Phi_{S_j}^k)^+ \Pi^\top \Phi_{S_i}^k g(s_l \Lambda_{S_i}^k). \quad (7)$$

We obtain the final functional mapping  $C_{ij}$  by combining  $C^l$  from the landmarks transformation and  $C_k^r$  reconstructed under the functional space dimension  $k$ , which encompasses both spatial and spectral domain information:

$$C_{ij} = \alpha C_{ij}^l + (1 - \alpha) C_k^r, \quad (8)$$

where  $\alpha$  is a trade-off parameter. Subsequently,  $C_{ij}$  is transformed into  $T_{ij}$  by NN search and encoded as  $\Pi$ , and the threshold  $\epsilon$  of LMD is gradually reduced in iterations to obtain more accurate landmarks. We summarize the whole process in Algorithm 1.

### Cycle Consistency Refinement

Following the pairwise correspondences optimization, we generate a cycle consistency basis from the graph  $\mathcal{G} = (\mathcal{V}, \mathcal{E})$  and then further optimize the consistency of  $C_{ij}$ .

**Cycle Consistency Basis Generation** Generating a cycle-consistency basis consists of three steps (Guibas, Huang, and Liang 2019). The first step is to construct the super-set cycle set  $\mathcal{C}_{\text{sup}}$ . We begin by constructing the breadth-first spanning tree  $\mathcal{T}$  rooted at each vertex  $v_i \in \mathcal{V}$ . From this tree, we derive a minimal cycle consistency basis  $\mathcal{C}(v_i) = \bigcup_{e \in \mathcal{E} \setminus \mathcal{T}} c_e$ . Specifically, for each edge pair  $e = (i, j) \in \mathcal{E} \setminus \mathcal{T}$ , we obtain the cycle  $c_e = (i, j) \sim p_{ji}$ , where  $p_{ji}$  is the unique path from  $j$  to  $i$  on  $\mathcal{T}$ . Subsequently, we construct  $\mathcal{C}_{\text{sup}} := \bigcup_{v_i \in \mathcal{V}} \mathcal{C}(v_i)$  and set  $\mathcal{C}_{\text{min}}$  to be the minimum depth cycle consistency basis.

Next, let  $v_e \in \{0, 1\}^{|\mathcal{E}|}$  be the indicator vector for edge  $e$  and denote  $v_c = \sum_{l=1}^k v_{(i_l, i_{l+1})}$  (where  $i_{k+1} = i_1$ ) as the indicator vector for cycle  $c = (i_1, i_2 \dots, i_k, i_1)$ . We optimize cycle weights  $\omega_c$  by formulating the following program:

$$\begin{aligned} \min_{\omega_c \geq 0, s_1, s_2} \quad & s_2 - s_1 \\ \text{s.t.} \quad & \begin{cases} s_1 \mathbf{I} \leq \sum_{e \in \mathcal{E}} v_e v_e^\top + \sum_{c \in \mathcal{C}_{\text{sup}}} \omega_c v_c v_c^\top \leq s_2 \mathbf{I}, \\ \sum_{c \in \mathcal{C}_{\text{sup}}} |v_c|^2 \omega_c = \theta, \\ \omega_c \geq \delta, \forall c \in \mathcal{C}_{\text{min}}, \end{cases} \end{aligned} \quad (9)$$

where the parameter  $\theta$  balances the loss and regularization terms. The solution of objective Eq. (9) follows the original work (Guibas, Huang, and Liang 2019).

Then, we control the cycle set size by importance sampling to ensure that the weighted sum of the sampled set  $\mathcal{C}_{\text{sample}} \subset \mathcal{C}_{\text{orig}} := \mathcal{C}_{\text{sup}} \setminus \mathcal{C}_{\text{min}}$  approximates that of the original set  $\mathcal{C}_{\text{orig}}$ . Let the maximum weight be  $\omega_{\text{max}} = \max_{c \in \mathcal{C}_{\text{orig}}} \omega_c$  and consider proper size  $M$  for  $\mathcal{C}_{\text{sample}}$ . Choose  $\eta \leq 1$  such that  $M \leq \sum_{c \in \mathcal{C}_{\text{orig}}} (\omega_c / \omega_{\text{max}})^\eta$ . We define an independent random variable  $x_c$  taking values as:

$$x_c = \begin{cases} 1, & \text{with } p_c, \\ 0, & \text{with } 1 - p_c. \end{cases} \quad (10)$$

Subsequently, the weights  $\bar{\omega}_c$  of each cycle  $c$  are corrected:

$$\bar{\omega}_c = \omega_c / p_c, \quad p_c := M \cdot \omega_c^\eta / \sum_{c \in \mathcal{C}_{\text{orig}}} \omega_c^\eta. \quad (11)$$

Finally, we obtain the sampled  $\mathcal{C}_{\text{sample}}$  as the cycle consistency basis.

**Consistent Constraint Formulation** With the cycle-consistency basis generated, we derive the consistent functional mapping  $C_{ij}, (i, j) \in \mathcal{E}$  by solving the following problem:

$$\begin{aligned} \min_{C_{ij}} \frac{1}{|\mathcal{E}|} \sum_{(i, j) \in \mathcal{E}} \|C_{ij} - C_{ij}^0\|_F^2 + \beta \sum_{(i, j) \in \mathcal{E}} \|C_{ij}^\top C_{ij} - \mathbf{I}\|_F^2 \\ + \mu \sum_{c=\{i_1 \dots i_k i_1\} \in \mathcal{C}} \omega_c \|C_{i_1 i_2} \dots C_{i_{k-1} i_k} C_{i_k i_1} - \mathbf{I}\|_F^2, \end{aligned} \quad (12)$$

where  $C_{ij}^0$  is the initial functional mapping optimized in the first step of our method,  $\omega_c$  are cycle weights, and  $\beta, \mu$  are the regularization parameters. The second term ensures the orthogonality of  $C_{ij}$ , and the third term constrains the cycle consistency.

**ADMM Optimization** Eq. (12) involves the product and summation operations of multiple matrices, and the last term, in particular, contains the concatenated multiplication of various matrices, making it complicated. For this reason, we use the alternating direction method of multipliers (ADMM) to solve it. Specifically, the augmented Lagrangian function of Eq. (12) is:

$$\begin{aligned} \mathcal{L}(C, Z, U) = \frac{1}{|\mathcal{E}|} \sum_{(i, j) \in \mathcal{E}} \|C_{ij} - C_{ij}^0\|_F^2 \\ + \beta \sum_{(i, j) \in \mathcal{E}} \|Z_{ij}^\top Z_{ij} - \mathbf{I}\|_F^2 + \mu \sum_{c \in \mathcal{C}} \omega_c \left\| \prod_{(i, j) \in c} Z_{ij} - \mathbf{I} \right\|_F^2 \\ + \sum_{(i, j) \in \mathcal{E}} \langle U_{ij}, C_{ij} - Z_{ij} \rangle + \frac{\rho}{2} \sum_{(i, j) \in \mathcal{E}} \|C_{ij} - Z_{ij}\|_F^2, \end{aligned} \quad (13)$$

where  $Z_{ij}$  is an auxiliary variable constrained by  $C_{ij} = Z_{ij}$  and  $U_{ij}$  is a Lagrange multiplier. Then,  $C_{ij}$ ,  $Z_{ij}$ , and  $U_{ij}$  are updated alternately until convergence:

$$C_{ij}^{k+1} = \frac{\sum_{(i, j) \in \mathcal{E}} C_{ij}^0 + \rho \sum_{(i, j) \in \mathcal{E}} (Z_{ij}^k - U_{ij}^k)}{|\mathcal{E}| + \rho}, \quad (14)$$

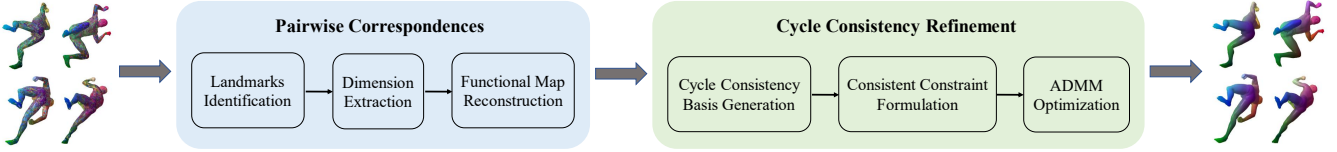


Figure 3: The schematic diagram illustrates the flow of our approach, divided into two parts: pairwise correspondences and cycle consistency refinement.

#### Algorithm 2: Overall Process of Our Approach

**Input:** Shape collection  $\mathcal{S} = \{S_i\}_{i=1}^n$ , initial correspondence  $\{T_{ij}\}_{i,j=1}^{n,n}$   
**Parameter:** Maximum iterations  $MaxIt$ , LMD thresholds  $\{\epsilon_{it}\}_{it=1}^{MaxIt}, \alpha$   
**Output:** Optimized  $C$

- 1: Model  $\mathcal{S}$  as a graph  $\mathcal{G} = (\mathcal{V}, \mathcal{E})$ ;
- 2: **for** every  $e_{ij}$  in graph  $\mathcal{G}$  **do**
- 3:   Obtain the optimized  $C_{ij}$  by Algorithm 1;
- 4: **end for**
- 5: Generate superset cycles  $\mathcal{C}_{\text{sup}}$ ;
- 6: Optimize cycle weights by Eq. (9);
- 7: Importance sampling to obtain cycles  $\mathcal{C}$  by Eq. (11);
- 8: Construct optimization problem for  $C$  by Eq. (12);
- 9: Formulate the Lagrangian function by Eq. (13);
- 10: **while** not convergence **do**
- 11:   Update Lagrangian variables by Eq. (14) - Eq. (16);
- 12: **end while**

$$Z_{ij}^{k+1} = \frac{\overline{Z_{ij}^k}}{\beta + \mu + \sum_{c \in \mathcal{C}} \omega_c},$$

$$\overline{Z_{ij}^k} = \mu \sum_{c \in \mathcal{C}} \omega_c \left( \prod_{(i,j) \in c} Z_{ij}^k - \mathbf{I} \right) + \sum_{(i,j) \in \mathcal{E}} (C_{ij}^k + U_{ij}^k)$$

$$+ \beta Z_{ij}^k ((Z_{ij}^k)^\top Z_{ij}^k - \mathbf{I}), \quad (15)$$

$$U_{ij}^{k+1} = U_{ij}^k + C_{ij}^{k+1} - Z_{ij}^{k+1}. \quad (16)$$

We empirically set the parameters  $\rho = 10^{-3}$ ,  $\beta = \mu = 1$ , and run ADMM until convergence. Finally, the overall process is summarized in Algorithm 2, with the final converged  $C$  as the output, and is visually represented in Fig. 3.

#### Parameter Setting

Our method introduces three hyperparameters,  $\alpha$ ,  $MaxIt$ , and  $\{\epsilon_{it}\}_{it=1}^{MaxIt}$ . The following explains how to set them.

Parameter  $\alpha$  balances the contributions of  $C_{ij}^l$  and  $C_{ij}^r$  in the final  $C_{ij}$  from Eq. (8) and varies from 0.1 to 0.9. We use the TOSCA (Bronstein, Bronstein, and Kimmel 2008) dataset as a test set to determine the appropriate value. As shown in Fig. 4, both relative geodesic error and cycle error are minimized when  $\alpha$  is set to 0.3.

Parameter  $\{\epsilon_{it}\}_{it=1}^{MaxIt}$  is the key threshold for determining landmarks at each iteration, with its length corresponding to the value of  $MaxIt$ . Empirically, We set  $\{\epsilon_{it}\}_{it=1}^{MaxIt} = [0.12, 0.1]$  and  $MaxIt = 2$ . This configuration balances

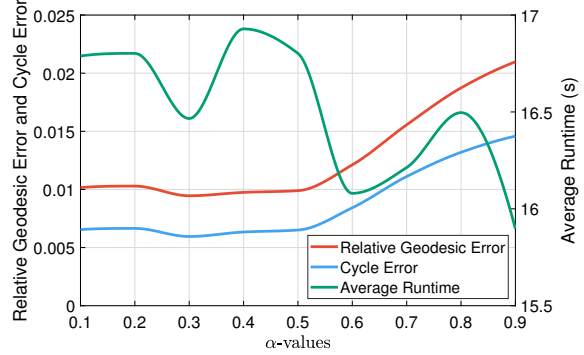


Figure 4: Parametric analysis of  $\alpha$ , including relative geodesic error (Red), average runtime (Green), and cycle error (Blue) of our method for different  $\alpha$  values.

geodesic error, cycle error, and runtime based on the Local Mapping Distortion values during actual runs.

## Experiments

In this section, we apply our method to challenging datasets and compare it with state-of-the-art methods.

#### Implement Details

**Dataset** Three public datasets are used in our evaluation experiments:

- **FAUST** (Bogo et al. 2014) contains 100 shapes representing 10 poses from 10 different human subjects, with each shape containing 6,890 vertices. For quantitative evaluation, we group the 10 poses of each subject into 10 independent shape collections.
- **SCAPE** (Anguelov et al. 2005) includes 71 shapes, each depicting a different pose of the same human subject, with each shape comprising 12,500 vertices. For quantitative analysis, we randomly select 10 shapes to create a shape set, resulting in a total of 7 shape sets.
- **TOSCA** (Bronstein, Bronstein, and Kimmel 2008) consists of 76 shapes across 8 categories, including both animal and human forms. Each shape contains approximately 10,000 vertices and includes ground truth data for benchmarking. For quantitative evaluation, we treat each category as an individual shape set.

**Evaluation** Our evaluation metrics include relative geodesic error to assess match accuracy and cycle error to evaluate cycle consistency.

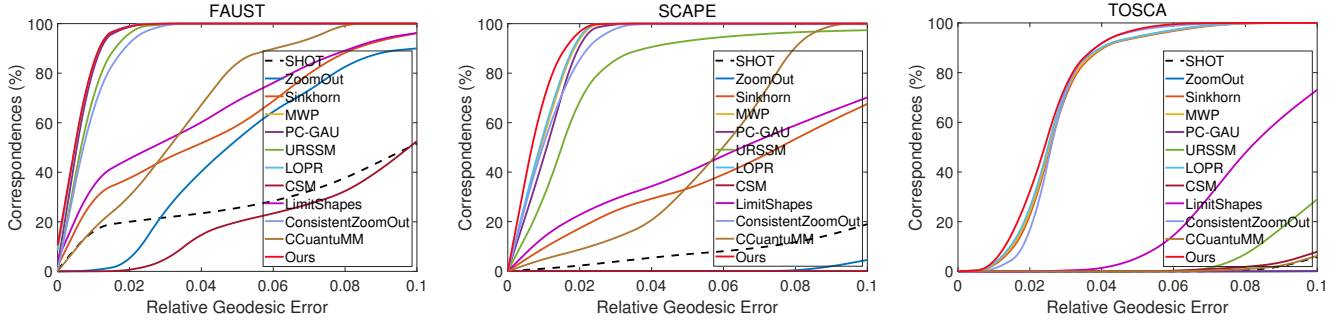


Figure 5: Evaluations of our method with other methods on FAUST, SCAPE, and TOSCA datasets with CQCs.

Methods	FAUST		SCAPE		TOSCA	
	Error	Cycle Error	Error	Cycle Error	Error	Cycle Error
Shape Matching Methods						
Zoomout	0.0563	0.0199	0.2257	0.0659	0.1940	0.0656
Sinkhorn	0.0392	0.0251	0.0776	0.0460	0.0275	0.0089
MWP	<u>0.0031</u>	<u>0.0015</u>	0.0092	0.0049	0.0270	0.0081
PC-GAU	0.0037	0.0022	0.0105	0.0060	0.1539	0.0569
URSSM	0.0066	0.0020	0.0211	0.0079	0.1440	0.0525
LOPR	<b>0.0030</b>	<u>0.0015</u>	<u>0.0089</u>	0.0048	0.0266	0.0079
Multi-Shape Matching Methods						
CSM	0.0954	0.0532	0.2589	0.1394	0.1543	0.0634
Limit Shapes	0.0337	0.0151	0.0704	0.0355	0.0880	0.0359
Consistent Zoomout	0.0081	0.0025	0.0117	<b>0.0027</b>	0.0272	<b>0.0031</b>
CCuantumMM	0.0316	0.0345	0.0559	0.0623	0.1226	0.0826
<b>Ours</b>	<b>0.0030</b>	<b>0.0014</b>	<b>0.0075</b>	<u>0.0034</u>	<b>0.0251</b>	<u>0.0066</u>

Table 1: Average relative geodesic errors and cycle errors of our method and state-of-the-arts on three public datasets, where the bold indicates the best and the underline indicates the second.

- **Relative Geodesic Error.** Following the Princeton benchmark protocol (Kim, Lipman, and Funkhouser 2011), matching accuracy is evaluated by calculating the geodesic distance between a matching pair  $(x, y)$  and the ground truth  $(x, y^*)$ , normalized by the diameter of shape  $\mathcal{Y}$ :  $\epsilon(x) = \frac{d_{\text{geo}}(y, y^*)}{\text{diam}(\mathcal{Y})}$ . The average relative geodesic error is reported, along with the Correspondence Quality Characteristic (CQC) curve showing the percentage of matches with relative geodesic error below  $r$ .
- **Cycle Error.** For point-to-point correspondences in a cycle  $c = \{S_1, S_2, \dots, S_{|c|}, S_1\}$ , the composite map  $T_{\text{cyc}} = T_{i_1 i_2} \circ \dots \circ T_{i_{|c|} i_1}$  is computed along the entire cycle. The cycle error is defined as the average geodesic distance between  $T_{\text{cyc}}$  and the identity map  $T_{\text{id}}$ , normalized by the cycle length:  $e_{\text{cyc}} = \frac{1}{|c|} \sum_i d_{\text{geo}}\{T_{\text{cyc}}(i), T_{\text{id}}(i)\}$ .

**Competitors** The competitor methods include shape matching methods like Zoomout (Melzi et al. 2019), Sinkhorn (Pai et al. 2021), MWP (Hu et al. 2021), PC-GAU (Colombo, Boracchi, and Melzi 2023), URSSM (Cao, Roet-

zer, and Bernard 2023) and LOPR (Xia et al. 2024), alongside multi-shape matching methods such as CSM (Huang and Guibas 2013), Limit Shapes (Huang et al. 2019), Consistent Zoomout (Huang et al. 2020), and CCuantumMM (Bhatia et al. 2023).

**Settings** The SHOT (Tombari, Salti, and Di Stefano 2010) descriptor space initializes MWP, PC-GAU, LOPR, Consistent Zoomout, and our method. Competitor methods use author-provided settings and code, with the number of eigenfunctions set to 500 or the maximum dimension of Zoomout and Consistent Zoomout upsampling iterations. Experiments are conducted on a desktop computer with a 3.50GHz Intel Core i9-9920X CPU and MATLAB R2018a, with GPU-accelerated K-nearest neighbor searches.

## Results Analysis

The quantitative evaluations on three public datasets, including CQC curves, relative geodesic errors, and cycle errors, are presented in Fig. 5 and Table 1. LOPR(Xia et al. 2024), as a pairwise shape matching method, performs well by re-

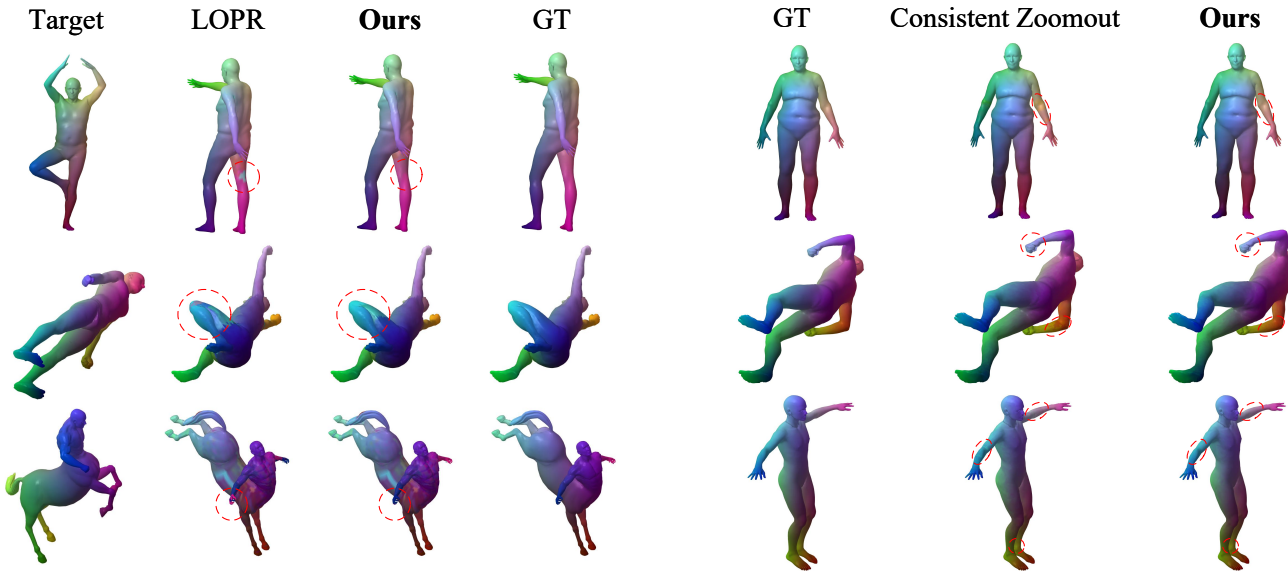


Figure 6: Comparison of qualitative results using color transfer on shape pairs between our method and LOPR. The first and last columns denote the target and source shapes with ground truth, respectively. Rows correspond to shapes from FAUST (top), SCAPE (middle), and TOSCA (bottom).

Methods	FAUST	SCAPE	Centaur	Wolf
#Vertices	6890	12500	10000	4344
Zoomout	13.2	56.9	22.0	6.6
MWP	1.9	12.0	3.4	1.5
LOPR	4.9	14.7	4.0	0.9
CCuantumMM	18546	32308	14116	2130.9
<b>Ours</b>	23.8	59.8	27.3	7.1

Table 2: Average runtime (in seconds) comparing our method with state-of-the-art methods across different resolutions is reported for the FAUST, SCAPE, and TOSCA datasets (Centaur and Wolf).

covering pointwise maps using local constraints. However, its reliance on local information leads to increased errors when consecutive local mismatches occur within the shape set. Consistent Zoomout(Huang et al. 2020) demonstrates a notable advantage in reducing cycle errors, achieving high consistency and performance by introducing canonical consistent latent bases. Nevertheless, our method achieves lower error levels in most scenarios. Furthermore, Fig. 6 illustrates the superior matching accuracy of our method compared to LOPR on a pair of shapes, while Fig. 7 showcases its enhanced matching consistency against Consistent Zoomout within a shape collection. These visual comparisons emphasize the superior accuracy and consistency of our method.

Moreover, Table 2 displays the average runtime of different methods at different resolutions. While the runtime of our method is acceptable, there is still room for improvement, particularly due to the use of geodesic distance matrix.

Figure 7: Qualitative comparison results between our method and Consistent Zoomout using color transfer. The first column denote the identity mapping  $T_{\text{id}}$ , while the second and third columns display the composite mapping  $T_{\text{cyc}}$  for Consistent Zoomout and our method along the cycle  $c$ , respectively. Rows correspond to shapes from FAUST (top), SCAPE (middle), and TOSCA (bottom).

Model	I	II	III	IV	<b>Ours</b>
Error	0.0115	0.0255	0.0106	0.0117	0.0095
Cycle Error	0.0073	0.0174	0.0070	0.0078	0.0060

Table 3: Ablation study results without: (I) landmark points functional maps; (II) spectral domain upsampling to reconstruct functional maps; (III) cycle consistency refinement; (IV) local mapping distortion to determine dimension.

### Ablation Study

We conduct ablation experiments to analyze each component’s contribution, as shown in Table 3. The components are highly interdependent, with accuracy and consistency significantly declining if any are removed, especially the spectral domain upsampling module.

### Conclusion

In this paper, we presented a novel and efficient approach to multi-shape matching with a more concise cycle consistency formulation. By modeling shapes as directed graphs, we derived cycle consistency basis as constraints. The method employs a two-stage optimization: optimizing pairwise correspondence accuracy via landmarks and refining consistency through cycle consistency basis. Experiments on three benchmarks show that our method outperforms state-of-the-art techniques in accuracy and consistency. Additionally, ablation experiments validate the effectiveness of each component.

## Acknowledgments

This work was supported by the National Natural Science Foundation of China (62171327, 624B2107, 62371350, and 62276192).

## References

Aigerman, N.; Poranne, R.; and Lipman, Y. 2015. Seamless surface mappings. *ACM Transactions on Graphics (TOG)*, 34(4): 1–13.

Anguelov, D.; Srinivasan, P.; Koller, D.; Thrun, S.; Rodgers, J.; and Davis, J. 2005. Scape: shape completion and animation of people. In *ACM SIGGRAPH*, 408–416.

Bernard, F.; Thunberg, J.; Swoboda, P.; and Theobalt, C. 2019. Hippi: Higher-order projected power iterations for scalable multi-matching. In *Proceedings of the IEEE/CVF International Conference on Computer Vision*, 10284–10293.

Bhatia, H.; Tretschk, E.; Lähner, Z.; Benkner, M. S.; Moeller, M.; Theobalt, C.; and Golyanik, V. 2023. Ccuantumm: Cycle-consistent quantum-hybrid matching of multiple shapes. In *Proceedings of the IEEE/CVF Conference on Computer Vision and Pattern Recognition*, 1296–1305.

Bogo, F.; Romero, J.; Loper, M.; and Black, M. J. 2014. FAUST: Dataset and evaluation for 3D mesh registration. In *Proceedings of the IEEE Conference on Computer Vision and Pattern Recognition*, 3794–3801.

Bronstein, A. M.; Bronstein, M. M.; and Kimmel, R. 2008. *Numerical geometry of non-rigid shapes*. Springer Science & Business Media.

Burghard, O.; Dieckmann, A.; and Klein, R. 2017. Embedding shapes with Green’s functions for global shape matching. *Computers & Graphics*, 68: 1–10.

Cao, D.; Roetzer, P.; and Bernard, F. 2023. Unsupervised learning of robust spectral shape matching. *arXiv preprint arXiv:2304.14419*.

Colombo, M.; Boracchi, G.; and Melzi, S. 2023. Extracting a functional representation from a dictionary for non-rigid shape matching. *Computers & Graphics*, 113: 43–56.

Gao, M.; Lahner, Z.; Thunberg, J.; Cremers, D.; and Bernard, F. 2021. Isometric multi-shape matching. In *Proceedings of the IEEE/CVF Conference on Computer Vision and Pattern Recognition*, 14183–14193.

Guibas, L. J.; Huang, Q.; and Liang, Z. 2019. A condition number for joint optimization of cycle-consistent networks. *Advances in Neural Information Processing Systems*, 32.

Hartman, E.; Sukurdeep, Y.; Klassen, E.; Charon, N.; and Bauer, M. 2023. Elastic shape analysis of surfaces with second-order sobolev metrics: a comprehensive numerical framework. *International Journal of Computer Vision*, 131(5): 1183–1209.

Hu, L.; Li, Q.; Liu, S.; and Liu, X. 2021. Efficient deformable shape correspondence via multiscale spectral manifold wavelets preservation. In *Proceedings of the IEEE/CVF Conference on Computer Vision and Pattern Recognition*, 14536–14545.

Huang, Q.; Wang, F.; and Guibas, L. 2014. Functional map networks for analyzing and exploring large shape collections. *ACM Transactions on Graphics (ToG)*, 33(4): 1–11.

Huang, Q.-X.; and Guibas, L. 2013. Consistent shape maps via semidefinite programming. In *Computer Graphics Forum*, volume 32, 177–186. Wiley Online Library.

Huang, R.; Achlioptas, P.; Guibas, L.; and Ovsjanikov, M. 2019. Limit shapes—a tool for understanding shape differences and variability in 3d model collections. In *Computer Graphics Forum*, volume 38, 187–202. Wiley Online Library.

Huang, R.; Ren, J.; Wonka, P.; and Ovsjanikov, M. 2020. Consistent zoomout: Efficient spectral map synchronization. In *Computer Graphics Forum*, volume 39, 265–278. Wiley Online Library.

Huber, D. F. 2002. *Automatic three-dimensional modeling from reality*. Carnegie Mellon University.

Jiang, L.; Lee, C.; Teotia, D.; and Ostadabbas, S. 2022. Animal pose estimation: A closer look at the state-of-the-art, existing gaps and opportunities. *Computer Vision and Image Understanding*, 222: 103483.

Kavitha, T.; Liebchen, C.; Mehlhorn, K.; Michail, D.; Rizzi, R.; Ueckerdt, T.; and Zweig, K. A. 2009. Cycle bases in graphs characterization, algorithms, complexity, and applications. *Computer Science Review*, 3(4): 199–243.

Kezurer, I.; Kovalsky, S. Z.; Basri, R.; and Lipman, Y. 2015. Tight relaxation of quadratic matching. In *Computer Graphics Forum*, volume 34, 115–128. Wiley Online Library.

Kim, V. G.; Lipman, Y.; and Funkhouser, T. 2011. Blended intrinsic maps. *ACM Transactions on Graphics (TOG)*, 30(4): 1–12.

Kovnatsky, A.; Bronstein, M. M.; Bronstein, A. M.; Glashoff, K.; and Kimmel, R. 2013. Coupled quasi-harmonic bases. In *Computer Graphics Forum*, volume 32, 439–448. Wiley Online Library.

Leonardi, N.; and Van De Ville, D. 2013. Tight wavelet frames on multislice graphs. *IEEE Transactions on Signal Processing*, 61(13): 3357–3367.

Melzi, S.; Ren, J.; Rodola, E.; Sharma, A.; Wonka, P.; and Ovsjanikov, M. 2019. Zoomout: Spectral upsampling for efficient shape correspondence. *arXiv preprint arXiv:1904.07865*.

Nogneng, D.; and Ovsjanikov, M. 2017. Informative descriptor preservation via commutativity for shape matching. In *Computer Graphics Forum*, volume 36, 259–267. Wiley Online Library.

Ovsjanikov, M.; Ben-Chen, M.; Solomon, J.; Butscher, A.; and Guibas, L. 2012. Functional maps: a flexible representation of maps between shapes. *ACM Transactions on Graphics (ToG)*, 31(4): 1–11.

Pai, G.; Ren, J.; Melzi, S.; Wonka, P.; and Ovsjanikov, M. 2021. Fast sinkhorn filters: Using matrix scaling for non-rigid shape correspondence with functional maps. In *Proceedings of the IEEE/CVF Conference on Computer Vision and Pattern Recognition*, 384–393.

Rodolà, E.; Cosmo, L.; Bronstein, M. M.; Torsello, A.; and Cremers, D. 2017. Partial functional correspondence. In *Computer Graphics Forum*, volume 36, 222–236. Wiley Online Library.

Sahillioglu, Y. 2020. Recent advances in shape correspondence. *The Visual Computer*, 36(8): 1705–1721.

Shoham, M.; Vaxman, A.; and Ben-Chen, M. 2019. Hierarchical functional maps between subdivision surfaces. In *Computer Graphics Forum*, volume 38, 55–73. Wiley Online Library.

Tombari, F.; Salti, S.; and Di Stefano, L. 2010. Unique signatures of histograms for local surface description. In *Proceedings of the European Conference on Computer Vision*, 356–369.

Van Kaick, O.; Zhang, H.; Hamarneh, G.; and Cohen-Or, D. 2011. A survey on shape correspondence. In *Computer Graphics Forum*, volume 30, 1681–1707. Wiley Online Library.

Wang, F.; Huang, Q.; and Guibas, L. J. 2013. Image co-segmentation via consistent functional maps. In *Proceedings of the IEEE International Conference on Computer Vision*, 849–856.

Xia, Y.; Lu, Y.; Gao, Y.; and Ma, J. 2024. Locality Preserving Refinement for Shape Matching with Functional Maps. In *Proceedings of the AAAI Conference on Artificial Intelligence*, volume 38, 6207–6215.

Xiang, R.; Lai, R.; and Zhao, H. 2020. Efficient and robust shape correspondence via sparsity-enforced quadratic assignment. In *Proceedings of the IEEE/CVF Conference on Computer Vision and Pattern Recognition*, 9513–9522.

Xiang, R.; Lai, R.; and Zhao, H. 2021. A dual iterative refinement method for non-rigid shape matching. In *Proceedings of the IEEE/CVF Conference on Computer Vision and Pattern Recognition*, 15930–15939.